



A Laser-induced Fluorescence Instrument for Detecting Tropospheric OH and HO₂: Characteristics and Calibration

IAN C. FALOONA^{1,2}, DAVID TAN^{1,3}, ROBERT L. LESHER¹,
NATHAN L. HAZEN⁴, CHRISTOPHER L. FRAME⁵, JAMES B. SIMPAS¹,
HARTWIG HARDER^{1,6}, MONICA MARTINEZ^{1,6}, PIERO DI CARLO^{1,7},
XINRONG REN¹ and WILLIAM H. BRUNE^{1*}

¹*Department of Meteorology, Pennsylvania State University, 503 Walker Building, University Park, PA 16802, U.S.A., e-mail: brune@essc.psu.edu*

²*Now at Department of Land, Air and Water Resources, University of California at Davis, Davis, CA, U.S.A.*

³*Now at School of Earth and Atmospheric Sciences, Georgia Institute of Technology, Atlanta, GA, U.S.A.*

⁴*Greenland, NH, U.S.A.*

⁵*ILC Dover, Inc., Frederica, DE, U.S.A.*

⁶*Now at Max-Planck-Institut für Chemie, D-55116 Mainz, Germany*

⁷*CETEMPS, Dipartimento di Fisica, Università degli Studi di L'Aquila, Coppito, Italy*

(Received: 11 September 2003; accepted: 19 November 2003)

Abstract. Measurement capability for the detection of atmospheric OH and HO₂ has been developed at the Pennsylvania State University over the last decade. The instrument is used in two forms: an aircraft configuration, Airborne Tropospheric Hydrogen Oxides Sensor (ATHOS), and the configuration used on towers, Ground-based Tropospheric Hydrogen Oxides Sensor (GTHOS). The instrument uses ultraviolet laser induced fluorescence (LIF) to detect OH in air that is pulled by a vacuum pump through a small inlet into a low-pressure detection chamber; HO₂ is detected by reacting it with NO to form OH, which is detected by LIF in a second detection chamber. In the calibration, equal amounts of OH and HO₂ ranging from 0.15 pptv to 100 pptv are produced via photolysis of water vapor by the 185 nm emission from a low-pressure Hg lamp. Estimated absolute uncertainty at the 2σ confidence level is ±32% for both OH and HO₂. The dependence of the instrument detection sensitivity has been quantified for changes in ambient water vapor, pressure, laser power, and the flow velocity of ambient air past the inlet. During the last 7 years, the instrument has been deployed in multi-investigator intensive field studies 5 times on the NASA DC-8 aircraft and 8 times on ground-based towers. The descriptions in this manuscript detail our cumulative wisdom of the instrumental response and calibration techniques developed over this time.

Key words: calibration, hydroperoxy radical, hydroxyl radical, instrument, laser-induced fluorescence.

* Corresponding author.

1. Introduction

Nature has been extremely reluctant to directly divulge the abundance of its primary oxidant, the hydroxyl radical. Consequently, the detection of atmospheric OH has had a long and tortuous history (e.g., Brune *et al.*, 1992; Eisele and Bradshaw, 1993). Odd hydrogen radicals ($\text{HO}_x = \text{OH} + \text{HO}_2$) have long been identified as crucial photochemical components of the natural atmosphere (Levy, 1971; McConnell *et al.*, 1971), but accurate measurement of their exact concentrations have eluded researchers for many years. It has only been during the last decade or so that instruments have demonstrated successful OH measurement capability (e.g., Perner *et al.*, 1987; Eisele and Tanner, 1991; Hard *et al.*, 1992; Wennberg *et al.*, 1995; Stevens *et al.*, 1994; Mount and Harder, 1995; Holland *et al.*, 1995; Creasey *et al.*, 1997; Brune *et al.*, 1998; Kanaya *et al.*, 1999; Creasey *et al.*, 2001; Faloon *et al.*, 2001). Most OH measurements have been made on surface-based platforms.

Accurate calibration techniques have been one of the major obstacles in the road to OH measurements, particularly for *in situ* instruments. The extreme chemical reactivity of the OH radical makes any given laboratory preparation of a known concentration susceptible to heterogeneous wall loss and homogeneous scavenging by impurities within seconds. The extreme reactivity also results in small atmospheric OH concentrations – typically less than 10^7 molecules cm^{-3} – despite a large OH flux through the atmosphere.

This paper is a description of an instrument for measuring OH and HO_2 that we have developed over the last decade, its ground-based and airborne configurations, and our method for calibrations using water photolysis as a source of odd hydrogen radicals. It also summarizes some of our experimental diagnostics from the field and the laboratory. Tests for instrument interferences are presented in an accompanying manuscript (Ren *et al.*, this issue).

2. Instrument Description

The Penn State HO_x instrument uses the fluorescent assay by gas expansion (FAGE) technique originally developed by Hard *et al.* (1984). Earlier versions of the Penn State ground-based instrument have been described in detail elsewhere (Stevens *et al.*, 1994; Mather *et al.*, 1997). More recent versions use the same principles but use more advanced technology to achieve better performance, as described briefly by Tan *et al.* (2001a).

The instrument can be configured for airborne measurements as the Airborne Tropospheric Hydrogen Oxides Sensor (ATHOS), which was developed for the NASA DC-8 in 1996, or for tower-based studies as the Ground-based Tropospheric Hydrogen Oxides Sensor (GTHOS), which was developed in 1998. Schematics of ATHOS and GTHOS, shown in Figure 1, indicate that the two instruments share many of the same components. We will first discuss the common characteristics and then the characteristics that are unique to each.

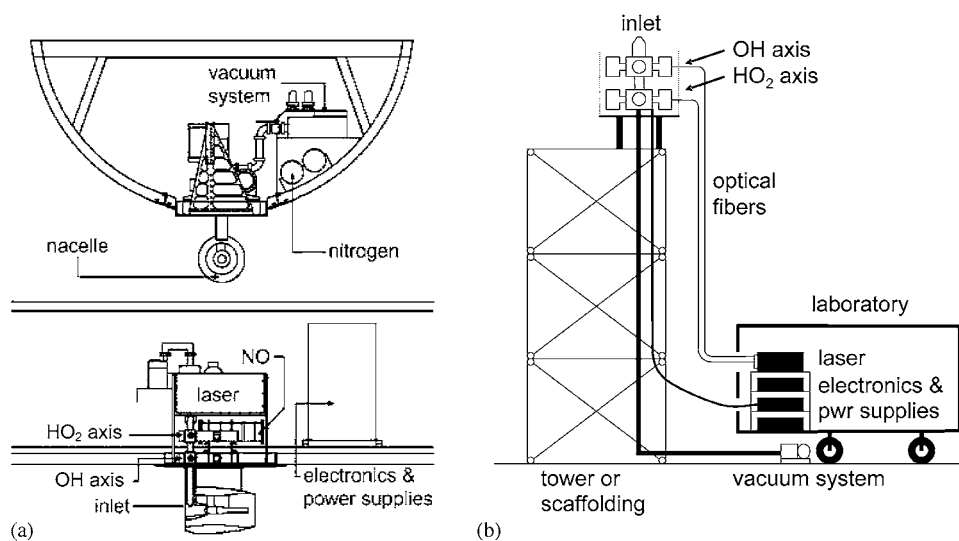


Figure 1. Schematics of ATHOS (a) and GTHOS (b). The views of ATHOS are looking aft from in front of the electronics rack (top) and from the DC-8's port side (bottom). In (b), the scaffolding used in different studies has been from 5 m to 40 m high.

2.1. CHARACTERISTICS COMMON TO ATHOS AND GTHOS

The instrument has four main subsystems: A low-pressure detection system, a laser, electronics for system control and data collection, and a vacuum system (Figure 1).

To sample the air, it is pulled by a vacuum pumping system through a small sharp-edged orifice (0.7–1.5 mm diameter) into a 5-cm diameter sampling tube that leads to the two detection axes in series. On the aircraft, a 1.5 mm diameter orifice is chosen so that the internal pressure of the system, which varies with the external pressure as the aircraft changes altitude, ranges from ~ 3 hPa at 12 km altitude to ~ 12 hPa on the ground. For GTHOS, a 1 mm orifice is usually chosen so that the internal pressure is 4–5 hPa. The vacuum pumping system consists of a supercharger (Eaton M-90, Cleveland, OH) backed by a rotary mechanical pump (Leybold D25B, Export, PA) and produces mass flow rates of ~ 10 L min^{-1} . Temperature is measured with a thermistor in the center of the sampling tube that joins the two detection axes, just below the OH axis. The detection cell pressure is measured by two sensors (MKS, 222, 10 Torr and 1000 Torr, Andover, MA).

Air encounters the OH detection axis first and the HO₂ detection axis second. In each detection axis, the air stream is probed by a pulsed laser beam. The wavelength of this laser beam corresponds to an $A^2\Sigma(v' = 0) \rightarrow X^2\Pi(v'' = 0)$ transition for OH, near 308 nm. Typically, the laser is tuned to the Q₁(2) transition, but the P₁(1) and Q₁(3) are also occasionally used. The laser beam is passed 32 to 40 times back and forth through the air stream with a White cell (White, 1942) that has mirrors (2.5 cm diameter) spaced 25 cm apart (Electro Optics, Inc.). At the center of the detection cell, each laser beam is approximately 3 mm high and

2–3 mm wide. All the beams together form a rectangle that is 6–8 mm high by 20 mm wide. The transmission through the White cell is greater than 92% with fresh optics. The laser power exiting the White cells is monitored by photodiodes (UDT, Inc., 555UV), as is the power exiting the laser system.

The weak OH fluorescence is detected by an electronically gated microchannel plate detector (Hamamatsu, R5916U-52, Hamamatsu City, Japan), which is set at right angles to both the air stream and the laser beam. As described in more detail below, the detector's high-gain state and signal pulse counters can be controlled by electronic gates. The optical train that feeds the detector includes two lenses (7.5 cm diameter, f1) and a narrowband interference filter (Barr Associates, Westford, MA). A concave spherical mirror collects fluorescence on the opposite side of the detection cell and sends it toward the lenses and detector. The total collection efficiency is estimated to be 5–8% (Brune *et al.*, 1995).

HO₂ cannot be detected directly by LIF. Instead, NO (nitric oxide, >99% Matheson, Twinsburg, OH) is added through a 2-cm diameter loop that is perforated with many small holes to the air flow between the two detection axes so that the HO₂ in the sample is rapidly converted to OH by the reaction: HO₂ + NO → OH + NO₂. This second measurement yields the total HO_x (OH + HO₂). HO₂ is the difference between HO_x and the OH measured in the first axis, scaled by the relative OH sensitivities of the two detection axes. The NO from commercial cylinders is passed at a regulated pressure of ~20 psi through an Ascarite-packed cylinder to remove higher oxide impurities. The NO flow rate is controlled by a series of sintered stainless steel flow restrictors (Mott Metallurgical, Farmington, CT) and solenoid closure valves (Clippard ES-2T-12, Cincinnati, OH). The usual flow rate is 5 standard cubic centimeters (sccm), but rates of 3 and 8 sccm are used during hourly calibration tests to ensure that the HO₂ conversion is maximized.

The 308 nm UV source is a tunable dye laser (Wennberg *et al.*, 1994) which is intracavity doubled and pumped by a diode-pumped Nd:YAG laser (from 1995 to 2000, LightWave Electronics, M210G-532-2500, Mountain View, CA; most recently, Spectra Physics, X30SC-1060A, Mountain View, CA). The pulse frequency is chosen to be 3 kHz; the pulse widths are 25–40 ns. The two laser assemblies are mounted on either side of a rigid vertical plate. The wavelength of the UV laser is tuned by means of an intracavity etalon (FSR 200 GHz) controlled by a stepper motor; the output beam alternates between an on-resonance frequency and off-resonance frequencies nearby (~30 GHz to either side). The laser line width is ~4.7 GHz, about 1.5 times the OH linewidth, as determined with a diagnostic etalon and photodiode that are mounted on the laser plate.

To monitor the laser wavelength and enable tuning the laser on-resonance and off-resonance, a small amount of laser light is passed through a low-pressure reference cell, in which a photomultiplier tube detects fluorescence from the copious OH that is made by thermolysis of water vapor on a 30-watt hot filament. Usually, the sample in the detection cell is probed at the on-resonance wavelength for 10 seconds followed by an off-resonance wavelength for 10 seconds. The

off-resonance period is used to determine the contribution to the signal from background effects. The off-resonance signal is monitored alternately at wavelengths greater than and less than the on-resonance wavelength.

Once the dye laser is aligned by adjusting the internal optics, it usually does not need to be aligned internally for weeks. The dye, Pyrromethene 597 (Exciton, Dayton, OH), is circulated through the dye laser from a 2-liter reservoir. Good dye laser power can be maintained for continuous operation during an entire month-long ground-based mission by occasionally adding a small amount of concentrated dye solution to the reservoir. The laser power tends to decrease as the aircraft ascends and descends or in the case of ground operations over the course of a day. It can be restored by adjusting the angle of the pump laser beam into the dye laser and by adjusting the pressure in the sealed dye laser cavity. The average laser power has been 10 to 25 mW.

The laser light is delivered to the detection system via fiber optic cables (200 μm diameter, Thor Labs, Munich, Germany). The laser beam from the dye laser is split so that 85% goes to the OH axis and 15% goes to the HO₂ axis. Each laser beam is focused into the end of a fiber. Near the detection chambers, the laser beam exiting the fiber is focused into the White cell. In ATHOS, the fibers are a meter long, but in GTHOS, they have been as long as 41 m, although 8–12 m fibers are typically used. The transmission of 308 nm laser light through the fiber is 0.98 m^{-1} , so that the laser transmission in the 41-m fiber was less than 0.4. In addition, reflections off the ends of the fibers create additional, smaller laser pulses that occur after the laser pulse at time intervals Δt (nanoseconds) = $9.8 \times$ the fiber length (m). These additional pulses cause laser scattering that must be avoided by using narrower detection on-gates, thus decreasing detection sensitivity when longer fibers are used.

An electronics block diagram is shown in Figure 2. The PSMCU is the power supply and motor control unit; the DAU is the data acquisition unit. The Windows-based computer uses Lab Windows graphing and menu routines. Sampling of all analog and digital signals occurs 5 times a second. The instrument operation uses an ASCII configuration file to set instrument operation. Many instrument functions are automated; a manual override allows for operator intervention. Both text and strip charts on flat panel displays are used to display data during operation. The instrument is controlled with a mouse and keyboard that can be some distance from the instrument, as it is in the aircraft configuration.

As soon as possible after the tail of the laser pulse exits the White cell, the microchannel plate detectors are electronically switched into a high gain state, increasing their gain by 8 decades. About 20 ns after the detector is switched to the high-gain state, the gates for the detector pulse counters are opened for 250–500 ns to collect the fluorescence signals. Another set of gated counters is opened while the detectors are in the low-gain state to observe the direct scattering from the laser pulse. This signal is proportional to the instrument detection sensitivity; its variation indicates variation of the detection sensitivity.

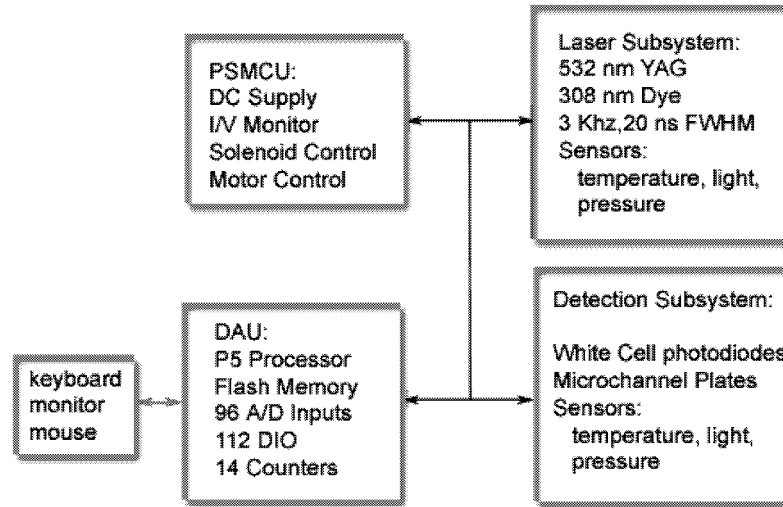


Figure 2. Block diagram of the electrical system for ATHOS and GTHOS.

Figure 3 depicts the timing of events as well as the shape of two theoretical fluorescent decays. The top (solid) curve represents an ideal decay at 4 hPa internal pressure in the absence of water vapor, and the lower curve (dashed-dot) corresponds to the same conditions but with 2% water. The total decay frequency, Γ , comprises the radiative decay frequency, γ_{nat} ($1/\gamma_{\text{nat}} = 688$ ns is the radiative, or natural, lifetime (Bailey *et al.*, 1997)), and the non-radiative decay frequency of the excited state by collisional deactivation with nitrogen, oxygen, and water molecules, which is described by the rate coefficients, k_{N_2} , k_{O_2} , and $k_{\text{H}_2\text{O}}$, respectively. The quenching rate coefficients and their temperature dependence were fitted to the expression: $k = a T^{1/2} - b T^{3/2} + c$. For publications until 1999, values from Copeland and Crosley (1986) for N_2 and O_2 and values from Wysong *et al.* (1990) for H_2O were used. After that date we have used values from Bailey *et al.* (1999) for H_2O , as in Table I.

The decay rate is proportional to the fluorescence intensity and is modeled as the equations:

$$\begin{aligned} \text{Intensity} &= [\text{OH}^*]_o \exp(-\Gamma t) \\ \Gamma &= \gamma_{\text{nat}} + k_{\text{N}_2}(T)[\text{N}_2] + k_{\text{O}_2}(T)[\text{O}_2] + k_{\text{H}_2\text{O}}(T)[\text{H}_2\text{O}], \end{aligned} \quad (1)$$

where $[\text{OH}^*]_o$ is the initial population of excited state OH ($A^2\Sigma$) established from the laser probe, t is time, $[\]$ denotes the number density of the enclosed chemical species, and the quenching rate coefficients have been written as functions of temperature, T , since their quenching efficiency increases at lower temperatures.

The instrument sensitivity is proportional to the shaded area in Figure 3, which is the fraction of the fluorescence that is detected. Therefore, in order to keep track of the sensitivity, it is necessary to keep track of the pressure, temperature, and the

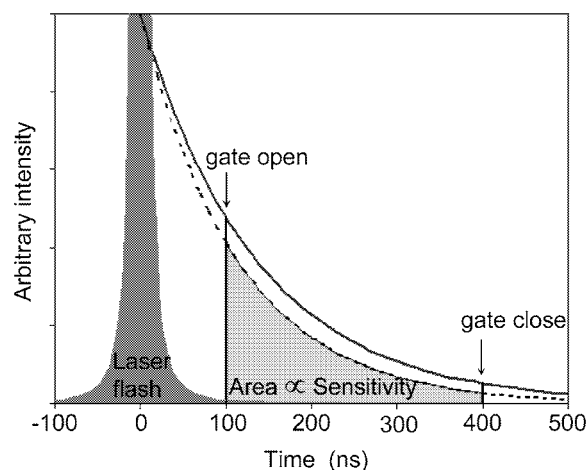


Figure 3. Schematic representation of the timing of photon counting process that is used to quantify OH concentrations in the Penn State LIF instrument. The fluorescence decays at 4 hPa and no water vapor is shown as the dark solid line, and the dash-dot curve represents the decay in the presence of 2% water vapor. The area under these curves is proportional to the instrumental sensitivity.

Table I. Quenching rate coefficients

Molecule	A (cm ² /K ^{1/2})	B (cm ² /K ^{3/2})	C (cm ²)
<i>Before 1999</i>			
N ₂	-1.668×10^{-11}	-1.731×10^{-14}	2.313×10^{-10}
O ₂	1.008×10^{-11}	1.655×10^{-14}	5.129×10^{-11}
H ₂ O	2.301×10^{-11}	1.115×10^{-12}	2.430×10^{-9}
<i>After 1999</i>			
N ₂	-1.668×10^{-11}	-1.731×10^{-14}	2.313×10^{-10}
O ₂	1.008×10^{-11}	1.655×10^{-14}	5.129×10^{-11}
H ₂ O	-4.017×10^{-10}	-4.469×10^{-13}	5.314×10^{-9}

water vapor mixing ratio at all times. At room temperature the quenching coefficient for oxygen is 4 times greater than that of nitrogen, so their contributions to Γ are about the same. Water quenches the excited state OH some 22 times greater than nitrogen, and thus can greatly reduce the detection sensitivity in environments like the moist marine boundary layer.

2.2. CHARACTERISTICS UNIQUE TO ATHOS

The NASA DC-8 aircraft travels at 200–240 m s⁻¹, as fast as 0.85 Mach. As a result, air around sampling inlets can easily become supersonic, potentially perturbing the sampling, particularly of a reactive constituent like OH. However, if the air speed at the sampling inlet can be reduced to a few 10's of m s⁻¹, unperturbed sampling is more likely. Reducing the air speed at the ATHOS inlet was accomplished by housing the inlet in a dual nacelle designed by Kevin James at NASA Ames Research Center (Figure 1(a)). This dual nacelle consists of two concentric cylindrical airfoils and, at the rear of the inner nacelle, a movable centered bulb. The sampling orifice inlet protrudes 2 cm into the smaller, inner nacelle near the leading edge and the inner airfoil's stagnation point. By moving the centered bulb, called the center body, toward the rear of the inner nacelle, the air flow through the inner nacelle is restricted and the velocity at the orifice can be slowed to speeds between 8 and 40 m s⁻¹. A pitot tube, which is located on the side opposite of the inlet inside the inner nacelle, measures the velocity. Compression occurs inside the inner nacelle. As a result, the nacelle air pressure is 1.2 times ambient at low altitudes and 1.5 times ambient at 12 km.

To ensure the proper operation of the dual nacelle, it was placed outside of the aircraft boundary layer. This offset forced the sampling tube to be 45 cm long, reaching from the sampling orifice inside the inner nacelle to the OH detection axis, which is mounted inside the aircraft, 1 cm above the aircraft's skin. In such a long tube, ~40% of the OH and ~10% of the HO₂ is lost to the walls. This wall loss is taken into account by the calibration.

2.3. CHARACTERISTICS UNIQUE TO GTHOS

The principal components of the system are widely separated in the GTHOS configuration. The detection module of GTHOS is contained in a thin sheet-metal enclosure (0.56 × 0.66 × 0.60 m), usually on a tower, while the laser and data acquisition system are housed in an air conditioned laboratory or trailer at the tower's base. Long electrical cables, gas tubing, and vacuum hose, as well as optical fibers, connect the laser and electronics in the trailer to the detection assembly, which is bolted to the tower.

For GTHOS, the inlet points up, rising 10 cm above the module housing. The OH detection axis is only 7 cm below the module housing. Because the air stream is still expanding when it reaches the OH detection axis, no significant OH or HO₂ are lost to the sampling tube walls in the 17 cm between the inlet and the OH detection axis. Any rain that enters the inlet causes large scattering signal spikes, but otherwise does no damage.

3. Calibration Method

3.1. THEORY

The calibration is based on quantitative production of equal parts OH and HO₂ by the vacuum-UV photolysis of water vapor:



The M in the latter reaction represents any molecule of the ambient gas, which acts to remove the excess internal energy of the combined translational energies of the reactants. The quantum yield for OH and H are both unity above 170 nm (Sander *et al.*, 2003). The water photolysis method has been employed by a number of researchers as a radical source (Stevens *et al.*, 1994; Schultz *et al.*, 1995; Tanner and Eisele, 1995; Heal *et al.*, 1995; Hofzumahaus *et al.*, 1996). OH and HO₂ are produced outside the instrument, with quantitative concentrations given by

$$[\text{OH}] = [\text{HO}_2] = \mathfrak{S}_{185} \sigma_{\text{H}_2\text{O}} [\text{H}_2\text{O}] \varphi \Delta t, \quad (2)$$

where \mathfrak{S}_{185} is the actinic flux of 185 nm radiation, $\sigma_{\text{H}_2\text{O}}$ is the photolysis cross section of water vapor at the same wavelength, φ is the quantum yield of the photolysis, and Δt is the exposure time of the water vapor to the light source. Parity of the OH and HO₂ yields is frequently checked in the laboratory in the ground configuration, for which OH wall losses are negligible, by adding NO internally to ensure that the total HO_x signal is twice of OH signal, the latter measured at the OH axis without adding NO.

A calibration factor is obtained from the expression:

$$C = \frac{\Delta S}{\chi_{\text{OH}} P}. \quad (3)$$

ΔS is the difference signal (counts per second, cts s^{-1}) between the online and offline count rates, χ_{OH} is the calculated OH mixing ratio, equal to $[\text{OH}]$ from Equation (2) divided by $[\text{M}]$, the ambient number density, and P is the laser power monitored at the output of the White cell (mW). Thus, C is the sensitivity per mW of laser UV ($\text{cts s}^{-1} \text{ pptv}^{-1} \text{ mW}^{-1}$), and CP is the total sensitivity. Subsequent measurements of χ_{OH} are then calculated by simply inverting Equation (3). Mixing ratio units (pptv) are used in the sensitivity and resultant radical abundances because the mixing ratio is the quantity that is conserved from outside the inlet to the low pressures inside the detection cell.

3.2. CALIBRATION PROCEDURE

The calibration system was designed to deliver the generated HO_x to the inlet system at transverse velocities on the order of what is experienced in flight, about 10 m s⁻¹ (Figure 4). The gas stream begins with ultra-zero air that is run through a 500 ml cartridge containing Hopcalite (Callery, Pittsburg, PA) which catalytically oxidizes CO to CO₂ thereby reducing the rate of conversion of OH to HO₂ after formation by the reaction:



The flow rate is measured by a mass flow meter (MKS) and then a variable stream is diverted to a water bubbler to humidify the air. After mixing through several meters of tubing, a small portion of the flow (<1 slpm) is conducted to a differential, non-dispersive IR water analyzer (LI-COR, model 6262, Lincoln, NE) where 2.59 μm IR absorption is used to quantify the water vapor concentration with an accuracy of ±2%. This water analyzer is routinely compared to a dew point hygrometer (General Eastern, 1311DR, Plainville, Connecticut). The bulk of the calibration air is sent into what is called the wand, a 1.27 × 1.27 × 30 cm square aluminum tube that is manufactured with three 3.8 cm long Suprasil™ windows separated by equal distances.

The speed of the air flow through the tube is greater than 4.75 m s⁻¹, leading to Reynolds numbers of at least 4000. Because the calibrator is rectangular and portions of the interior are painted with coarse black paint, the flow is turbulent, and thus has a flat velocity profile. Measurements of the flow profile made with a pitot tube indicate that the velocity does not change more than 13% across the bulk of the cross sectional area, and the integrated flow rate agrees with that calculated from the mass flow measurement to within 6%.

The main concern about a turbulent flow is the higher efficiency with which the transport of the radicals to the walls takes place. By situating the Hg lamp module at each of the three windows in the calibrator consecutively, a measure of the wall loss within the calibrator can be extrapolated to the inlet of the instrument. Results of these types of tests indicate that the loss of OH to the walls of the calibrator during the 4–6 ms transit to the inlet, when the lamp module is in the full forward window, is less than 5%.

The Hg lamp module consists of one or two low pressure Hg lamps (Oriol, Stratford, CT) that are housed in an aluminum cartridge that can be mounted over one of the Suprasil™ windows on the wand. A two-lamp version was used until 1999; a one-lamp version is used now. The housing is continually purged with dry N₂. In both versions, thin-walled tubes (3 mm diam., 10 mm long) are packed together in front of the lamp to create an approximate plane parallel UV field. The tubes are painted with a black, low-fluorescent paint (IIT, Chicago, IL) to absorb all light except the light that passes directly down the tubes. These tubes partially collimate the 185 nm light, providing a more uniform actinic flux distribution in the photolysis region.

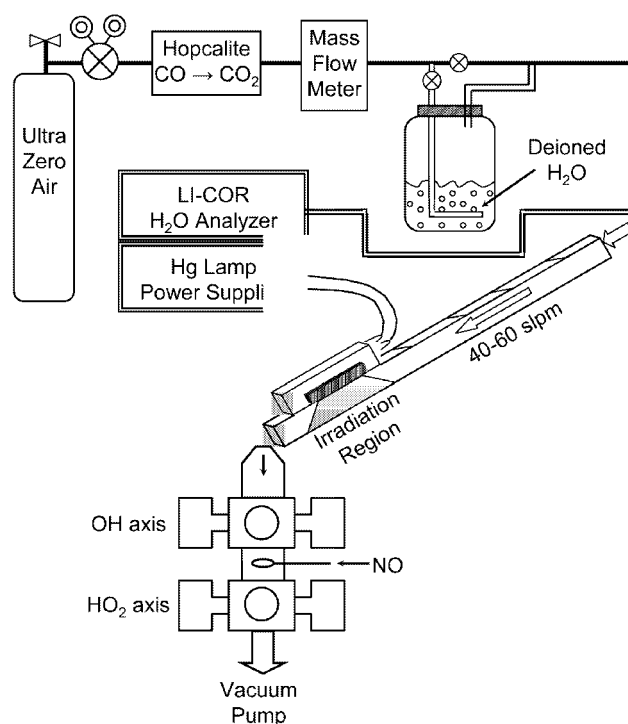


Figure 4. Schematic illustrating the principal components of the portable HO_x calibration system. The water vapor in humidified ultra-zero air is measured and irradiated with the 185 nm radiation from Hg lamps to produce quantitative and equal concentrations of OH and HO₂.

By varying the water vapor mixing ratio, Hg lamp supply current, and flow speed in the calibrator, the amount of OH (and the equivalent HO₂) can be adjusted from 0.15 pptv ($\sim 3.5 \times 10^6$ molecules cm⁻³) to 100 pptv ($\sim 2.5 \times 10^9$ molecules cm⁻³), spanning almost three decades. The mass flow rate through the calibrator is an important quantity because it determines the velocity and thus the exposure time in the calibrator. Although the instrument ingests less than 15 standard liters per minute (slpm) at 1000 hPa ambient pressure, the interface between the calibrator outlet and the inlet orifice is open. Tests show that a minimum of about 40 slpm is required to overfill the volume near the inlet sufficiently to achieve quantitative transfer of the HO_x, as seen in Figure 5.

When the HO_x instrument is on the ground or a tower, its internal pressure remains effectively constant. Thus, the calibrations are done at the same conditions as the measurement. However, when the instrument is on the aircraft, its internal pressure varies from ~ 12 hPa to ~ 3 hPa. Since the change in the internal pressure can alter the detection sensitivity, ATHOS must be calibrated over the same range of internal pressures. This is accomplished by calibrating ATHOS repeatedly with orifices of different sizes in order to achieve internal pressures over the entire range

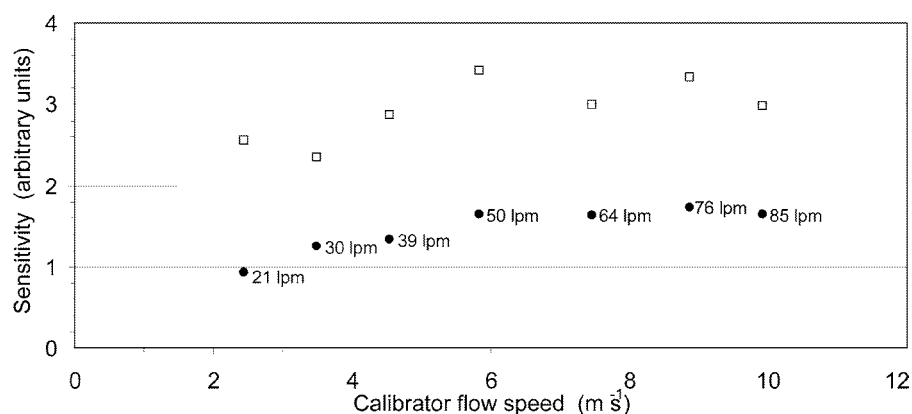


Figure 5. Calibration results illustrating the dependence of the sensitivity versus the transverse flow speed as controlled by the flow rate in the calibrator. The filled symbols are the OH signal; the open symbols are the signals from OH and HO₂ from the calibrator.

that will be encountered during flight. This method of calibration assumes that the losses of OH and HO₂ on the surface of the different inlets are small and constant. We discuss tests of this assumption in Section 4.6.

Quantifying [OH] and [HO₂] requires knowledge of each term on the right-hand side of Equation (2). Our primary calibration technique has been to quantify each term individually, including the absolute 185 nm flux and the exposure time, and then multiply them together. Another commonly used approach is to use an actinometer to determine the overlap of the 185 nm light and the exposure time. Both absolute flux measurements and actinometry are now used in the calibrations.

3.3. ABSOLUTE FLUX CALIBRATION

The UV flux from the lamp module was periodically checked with two solar blind Cs-I phototubes (Hamamatsu, R1180, Hamamatsu City, Japan). The response of these photodiodes to 185 nm emissions is determined by comparison with a solar blind Cs-I photomultiplier tube (RSI model 231–209, Baltimore, MD) that was calibrated at the Laboratory for Atmospheric and Space Physics in Boulder, CO. The PMT was calibrated to a relative uncertainty of less than 5% in the EOS-SOLSTICE detector calibration chamber, CTE2, using a Hamamatsu deuterium lamp and an Acton VM502 monochromator (Acton, MA) equipped with a NIST traceable EVSD photodiode detector (Science Applications Inc., McLean, VA). The PMT is used as a secondary transfer standard, while the photodiodes are the working standards.

The absolute sensitivity of the photodiodes is found by placing each in turn side-by-side with the absolutely calibrated PMT and exposing them both to light from an Hg lamp that is positioned directly in front of the photodiode and then the PMT. The light from the Hg lamp is collimated with apertures. Apertures are

also placed in front of the photodiode and PMT. Because the PMT is much more sensitive than the photodiodes, neutral density filters with an optical density of ~ 3 are also placed in front of the PMT. To ensure that the photodiode calibration is robust, many factors are varied, including the distance between the lamp and the photodiode and PMT, the lamp current, and the aperture sizes. Calibrations performed in laboratory air and in nitrogen inside a Teflon enclosure produce the same results.

A second part of this procedure is the mapping of the 185 nm flux from the lamp module that is used in the calibration. The lamp module is bolted to an optical table. The photodiode with a small aperture is fixed to a mount that can be translated over 3 axes. The flux mapping is done at three distances from the lamp, corresponding to the front, middle, and back of the 0.5" calibration tube; typically more than 70 measurements are taken to map each plane. These measurements are then combined to give the actinic flux in the photolysis zone of the calibration tube. These two procedures are now done before the calibrations that preceded and follow each field study.

The greatest uncertainty with this technique is determining the actinic flux exposure from the overlap of the mapped actinic flux and the exposure time of water vapor to that actinic flux. However, the collimating tubes and lamp position produces an actinic flux field that is uniform to better than 20% until near the edges of the actinic flux field, where it falls off. A second concern is that the flux mapping on the optical bench does not give a good representation of the actinic flux within the calibrator. However, tests have shown that the 185 nm light is effectively absorbed by the black paint that is on the inside of the calibrator at each of the three optical axes along the wand's length. Thus, we believe that this calibration technique produces accurately known OH and HO₂ concentrations.

3.4. ACTINOMETRIC CALIBRATIONS WITH O₃ AND N₂O

Actinometric techniques measure directly the exposure of an air sample to UV light and thus account directly for the overlap between the UV flux and the exposure time of the air to that UV flux. All that is required is a gas that is photolyzed by 185 nm light, knowledge of the absorption cross section, and an instrument that accurately measures a photolysis product. While the absolute measurement of the actinic flux and these two actinometric methods each have their strengths and weaknesses, the agreement between these commonly used methods would give confidence in the absolute Hg actinic flux values.

In ozone actinometry, the Hg line at 185 nm photolyzes O₂ to make two O atoms, which immediately react with O₂ to form O₃ (Holland *et al.*, 1998; Creasey *et al.*, 2000). The ozone is sampled from air that is passed through our calibrator with an NO_x analyzer (TEI, 42C, Franklin, MA) that is reconfigured so that excess reagent NO is added instead of reagent O₃. The NO_x analyzer was calibrated at higher O₃ levels before the measurements with an O₃ analyzer (TEI, 49C, Franklin,

MA), which itself had been calibrated against a primary standard O₃ calibrator (TEI, 49C-PS, Franklin, MA). Because the effective absorption cross section depends strongly on the Hg 185 nm line shape (Lanzendorf *et al.*, 1997), the effective O₂ cross section is measured by varying the O₂ mixing ratio in an absorption tube prior to the calibration. This cross section is typically 1.1×10^{-20} cm². A second difficulty with this technique is that the amount of ozone produced in the calibrator is 1–2 ppbv, which is not substantially larger than the increased uncertainty in the zero value of the NO_x analyzer that is reconfigured to detect O₃, which is not its normal use.

In N₂O actinometry, the Hg line at 185 nm photolyzes N₂O to make N₂ and O(¹D), with a quantum yield of 1.0 (Sander *et al.*, 2003). The O(¹D) reacts rapidly with N₂O to form 2 NO molecules (Edwards *et al.*, 2003). The resulting NO is then detected with an NO_x analyzer (TEI, 42C). When the N₂O mixing ratio is 0.20, the amount of NO that is produced is 1.6 ppbv. This amount of NO is well above the detection limit for the NO_x analyzer used in its normal configuration of detecting NO. The NO_x analyzer is calibrated just before the calibration with an NO mixture that is certified by Matheson Tri-Gas. Because the N₂O absorption cross section is 1.43×10^{-19} cm², the 185 nm light is partially absorbed across the 1.27-cm calibrator tube. A correction for this absorption is applied as described by Edwards *et al.* (2003).

4. Sensitivity Dependence on Controlling Variables

4.1. THEORETICAL SENSITIVITY DEPENDENCES

The instrument sensitivity is greatly affected by the change in the instrument internal pressure, the water vapor concentration, and the laser power. Internal pressure and water vapor concentration influence the calibration through the three components: the internal number density of OH, [OH]_{int}, which increases linearly with internal pressure at a constant temperature for a constant OH mixing ratio; the collisional quenching effects manifest in Equation (1), Q; and the OH transmission, Φ, which is the fraction of OH that survives loss on the sampling tube's walls and is detected at the detection axis. If we assume these effects are separable then the total sensitivity can be described by the product of three functions of the internal pressure, P_{int},

$$C(P_{\text{int}}) = D_1(P)\Phi Q[\text{OH}]_{\text{int}}. \quad (4)$$

Here D₁(P) is a lumped constant of all pressure-independent parameters, including laser power, which is determined from the calibration.

Pitot tube flow measurements made within the low-pressure inlet tube have established that the air entering the pinhole does not significantly contact the inlet tube's walls until ~20 cm downstream of the pinhole. Under steady-state conditions, the loss to the walls, represented by a reaction coefficient, *k_w*, is sustained by the radial molecular flux. According to Fickian principles, this flux is directly

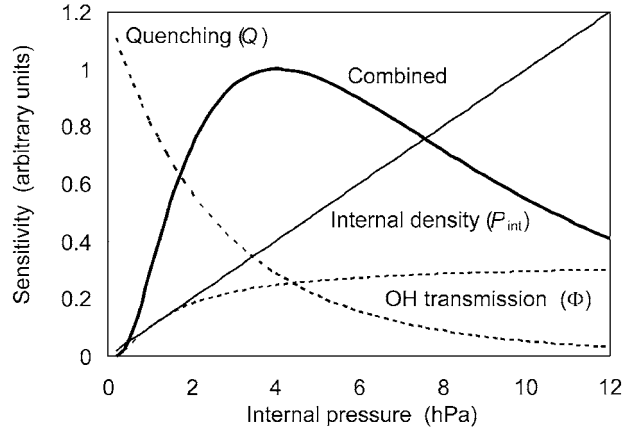


Figure 6. Three pressure dependent components of the LIF sensitivity: the internal density (gray solid line), OH transmission (gray dashed line), and quenching (dashed line). The product of these three functions (heavy solid line) is the expected form of the pressure dependent sensitivity.

proportional to the gas diffusion coefficient, D_g , of the reactive species in question. Furthermore, because the diffusion coefficient is inversely proportional to the pressure, the wall loss is also: $k_w \propto D_g \propto 1/P_{\text{int}}$. The wall loss function then takes the form

$$\Phi(P_{\text{int}}) \propto \exp(-k_w t_r) = \exp(-D_2/P_{\text{int}}) \approx 1 - D_2/P_{\text{int}}, \quad (5)$$

where t_r is the transit time down the low pressure inlet tube. The volumetric flow rate through the instrument does not change significantly over the range of external pressures sampled during flight because the vacuum pump used has a constant displacement, so that the measured volumetric flow changes less than 10% for the pressure range used. Thus the transit time is independent of the external pressure. D_2 is a constant that includes t_r and the other (pressure independent) factors of k_w .

The quenching term, $Q(P_{\text{int}})$, is determined by integrating the decay rate equation (Equation (1)) over the interval set by the counter gates. Let g_1 and g_2 represent the times of gate opening and closure, respectively. Then the quenching pressure dependence is

$$Q(P_{\text{int}}) \propto \frac{e^{-\Gamma g_1} - e^{-\Gamma g_2}}{\Gamma}, \quad (6)$$

where Γ is the excited state decay frequency. The overall shape of this theoretical function is plotted in Figure 6 along with the three factors outlined above (normalized to appear together on the same graph). $Q(P_{\text{int}})$ can be calculated using the known gate timing g_1 and g_2 and using the published quenching coefficients for N_2 , O_2 and water vapor in Table I.

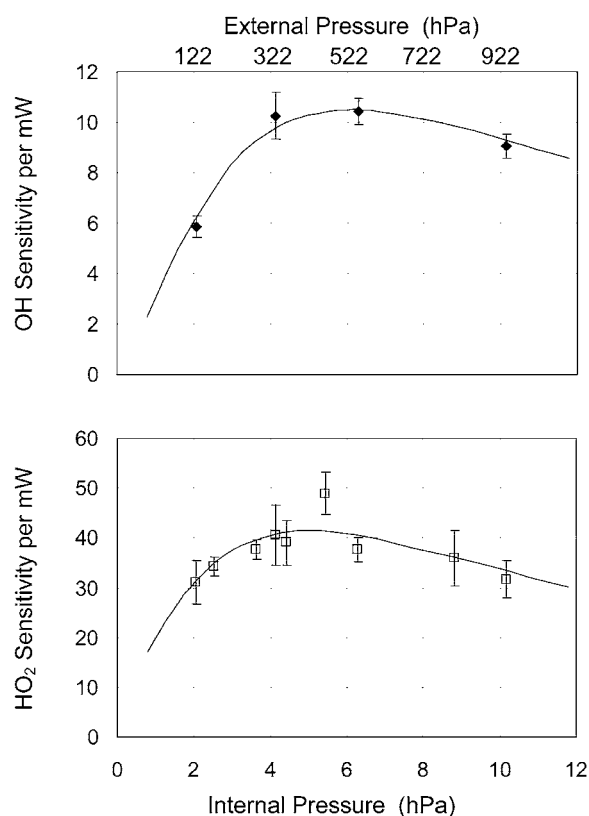


Figure 7. Detection sensitivity per mW for OH (top) and HO₂ (bottom) as a function of internal pressure of detection cell as well as of external pressure that reflects the sensitivity change with altitude for PEM Tropics B calibrations in 1999. The units are $\text{cts s}^{-1} \text{pptv}^{-1} \text{mw}^{-1}$. The error bars are the estimated precision (1σ) of each calibration and the solid lines are the fitted curves through the laboratory data using Equation (4).

4.2. FITTING THE CALIBRATION PRESSURE DEPENDENCE PRIOR TO JUNE, 1999

The sensitivity data at several pressures are used to fit a curve of the form given in Equation (4) using a least squares Levenberg-Marquardt method (Levenberg, 1944; Marquardt, 1963) to derive the main coefficient D_1 from Equation (4) and D_2 from Equation (5). Figure 7 illustrates the data and the curve for both OH and HO₂ sensitivities calibrated during the PEM-Tropics B deployment. The internal pressures have been converted to approximate atmospheric pressures outside of the aircraft to illustrate the sensitivity change with altitude. The error bars in the Figure 7 represent $\pm 1\sigma$ standard deviation of the precision of the sensitivity evaluated at each pressure. The relative precision is usually less than $\pm 10\%$ and is limited by unmonitored fluctuations in the calibration system, the uncertainty in the water correction, and to a lesser extent the Poisson counting noise of the measured signal.

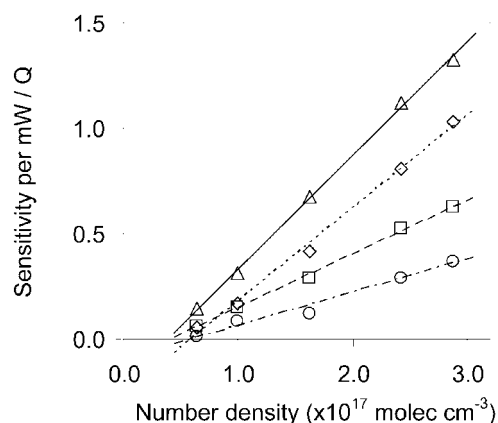


Figure 8. Calibration results performed for TRACE-P in spring 2001 using different sizes of inlets. Lines are the linear least squares fittings for OH and HO₂ sensitivities. Different symbols and fitted lines are for OH and HO₂ at two axes: triangles with solid line for HO₂ at OH axis; diamonds with dotted line for OH at OH axes; squares with dashed line for HO₂ at HO₂ axis; and circles with dash-dot line for OH at HO₂ axis.

The D_2 coefficient in Equation (5) represents the likelihood of wall loss on the way to the detection axes. The values found for OH are approximately 70% greater than the HO₂ values indicating a greater uptake coefficient on the inlet tube surface for OH. This behavior is evident in the sharper falloff in OH sensitivity at low pressures, as in Figure 7, where diffusion to the wall begins to dominate the sensitivity.

4.3. FITTING THE CALIBRATION PRESSURE DEPENDENCE AFTER JUNE, 1999

The term that is the most non-linear of all the terms in the sensitivity equation (Equation (4)) is quenching, Q . While $[\text{OH}]_{\text{int}}$ is absolutely linear with pressure, the wall loss term, Φ , has only a small pressure dependence above 2.5 hPa, the pressure range used for the measurements. This near-linearity in the absence of quenching suggests that linear least squares fitting procedure might give a more accurate representation of the calibration in the face of the random errors in the individual calibration data points. The calibration value can be retrieved with knowledge of the internal pressure and temperature and the water vapor concentration, which comes from simultaneous water vapor measurements from other research groups. Good linearity is achieved ($R^2 = 0.94\text{--}0.99$) in calibrations done for the NASA TRACE-P study in spring 2001 (Figure 8). Because of the greater freedom from ambiguity in the linear least squares fitting, this approach is deemed preferable to the non-linear fit used previously. This linear fit and the previously used non-linear fit give the same density dependence for the calibration to better than 10%, with the greatest difference occurring at the lowest density.

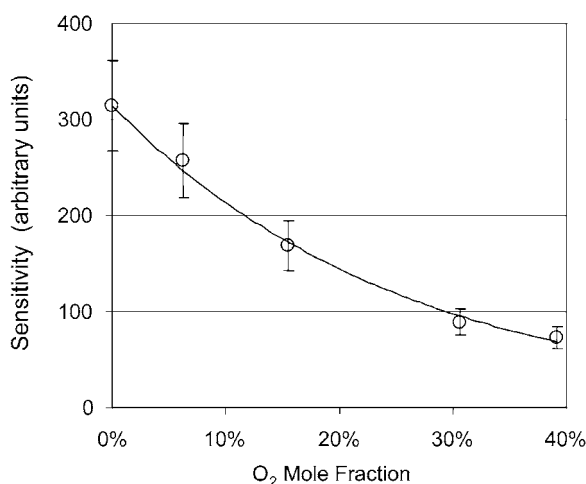


Figure 9. The OH sensitivity per mW as a function of oxygen mole percent. The data are from one lab experiment and the error bars represent the 1σ noise of each measurement. The solid line is the theoretical dependence of the sensitivity.

4.4. SENSITIVITY DEPENDENCE ON QUENCHING

Several tests were performed to ensure that the calibration factor varies as expected with changes in pressure, temperature, and water vapor. Water vapor quenching is the most variable and, for humid conditions in Earth's atmospheric boundary layer, can be greater than the quenching by nitrogen and oxygen combined. The effects of quenching on the detection sensitivity must be well understood and quantified in order to apply the correct calibration numbers.

First, the oxygen mole fraction was varied in the air supplied to the calibrator to test quenching by N_2 and O_2 , as in one test shown in Figure 9. The points are measurements and the solid line is the theoretical curve for changes in molecular oxygen mixing ratio at constant pressure and temperature. Although the starting point of the theoretical curve is arbitrarily chosen, the expected curvature due to O_2 quenching matches the instrumental response when all other conditions are held fixed. Thus the relative magnitudes of k_{O_2} and k_{N_2} as well as the theoretical description depicted in Figure 3 are supported by the experiment.

The usual and simplest method for changing the OH in the calibration wand is to change the amount of water vapor, which unfortunately changes both the OH and the water vapor quenching. Thus, a plot of C versus [OH] tends to decrease with increasing [OH] because of increased water vapor quenching (Figure 10). The theoretical water vapor quenching, using the fitted temperature-dependent quenching cross sections of Bailey *et al.* (1999), gives a good fit to the observations, while the theoretical curve using Wysong *et al.* (1990) does not. Thus, the issue of unexpected sensitivity decrease with additional water vapor (Mather *et al.*, 1997) appears to have been resolved for our instrument.

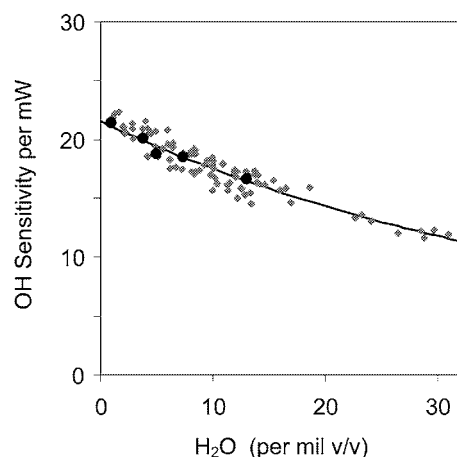


Figure 10. Comparison of water effect and theoretical expectation on OH sensitivity. The OH sensitivities (gray diamonds) obtained from field calibrations are plotted as a function of water concentrations in the calibrator. The solid line is theoretical quenching of the OH fluorescence by N₂, O₂, and H₂O from Equation (1) with the initial value (when [H₂O] = 0) equal to the intercept of the linear fitting for all points. Black solid circles show the example of the OH sensitivity dependency on H₂O mixing ratio when additional H₂O was added downstream of the photolysis zone.

Other FAGE experimentalists have seen an unexpected decrease in sensitivity with increasing water vapor, beyond that due to quenching. They have postulated that water cluster formation in the free-jet expansion beyond the orifice inlet removes OH, so that the effective sensitivity decreases non-linearly with more water vapor (Holland *et al.*, 1995; Hofzumahaus *et al.*, 1996; Creasey *et al.*, 1997). However, in the most recent version of their instrument, Holland *et al.* (2003) no longer observe this effect and instead see a smaller, linear decrease.

It is possible that OH production in our calibrator is not linearly dependent on water vapor. A test for this possibility is to fix the amount of water vapor flowing through the calibrator's photolysis zone and add a variable amount of water vapor downstream of the photolysis zone. As seen in Figure 10, the effects of increasing water vapor are the same whether water vapor is changed upstream or downstream of the photolysis zone, as would be expected if OH production was linearly dependent on water vapor in the photolysis zone.

The total decay frequency, Γ , can be measured directly in our instrument. The counter gates may be electronically scanned in 10 ns increments across approximately 300 ns of the fluorescence decay. These scans take only a few minutes in the laboratory or in flight. With constant conditions maintained, the counts in each 10 ns bin were then averaged and the data were fitted to an exponential curve to determine the excited state OH lifetime. Laboratory measurements of the lifetime in this fashion agree to within 2% of those calculated using Equation (1) for the condition in which water vapor is varied from 500 to 11,000 ppmv while pres-

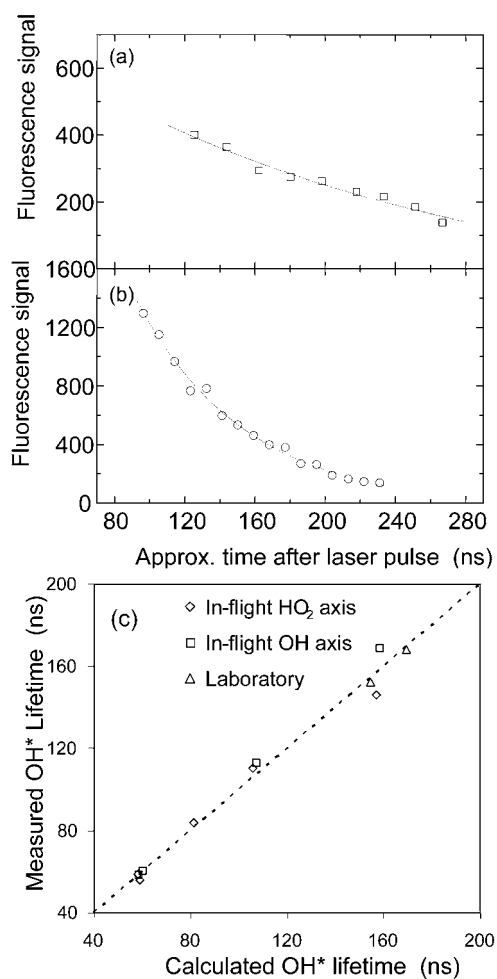


Figure 11. OH fluorescence decays measured during PEM-Tropics B. The top decay is from the flight of 18 April, 1999 at an altitude of 10.7 km with only 37 ppmv of water vapor and a theoretical lifetime is 157 ns (solid line). The ordinate is the number of photon counts collected over ten seconds in each 10 ns bin. The middle graph is a decay measured at 320 m above the ocean in the presence of >2.4% water and the theoretical lifetime was only 59 ns (solid line). The bottom graph is a plot of the measured vs. calculated lifetimes for several other periods during the mission as well as in the laboratory.

sure and temperature remain fixed (Figure 11c). Experimental confirmation of this agreement has also come in the atmosphere during the NASA Pacific Exploratory Mission – Tropics B (Figures 11(a, b)). Thus, our measured OH quenching agrees well with the quenching expected from theory for the large range of atmospheric conditions (Figure 11(c)).

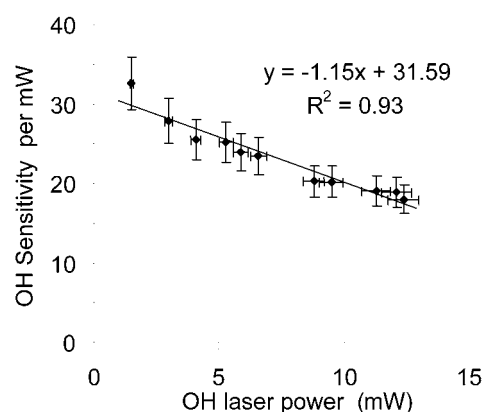


Figure 12. Sensitivity per mW decrease with increasing laser power. The measurements (symbols) are averaged with the standard deviations shown. A least squares fitting to the data shows a $\sim 4\%$ decrease in C per mW of laser power.

4.5. SENSITIVITY PER mW DEPENDENCE ON LASER POWER

The instrument sensitivity per mW appears to decrease linearly with laser power, even at a few mW, as in Figure 12. Because this decrease is linear with laser power and occurs for even a few mW of laser power, it does not result from the saturation of the OH electronic transition, as can happen with LIF detection (Ortgies *et al.*, 1981). Instead, it is likely a result of reduced sensitivity of the microchannel plate detector (MCP) as a function of exposure to light. While the OH fluorescence is weak, the Rayleigh and chamber scattering of the laser pulse subjects the photocathode to a strong light pulse. The decrease in the MCP's sensitivity per mW with increased laser power is likely related to the increased scattered light hitting the detector at greater laser powers. Fortunately, the effect is observed to be constant through frequent calibrations. Because of this laser power dependence, the laser power is noted during the calibration and the calibration factor, C, is then corrected for this observed degradation of $\sim 4\%$ per mW laser power in the computer program that calculates HO_x mixing ratios.

4.6. SENSITIVITY DEPENDENCE ON ANGLE OF ATTACK AND AIRFLOW VELOCITY

In the laboratory, the measured sensitivity is found to be independent, to within 10%, of the angle at which the calibrator flow tube is oriented with respect to the inlet. This invariance implies that any OH loss on the inlet's external surface has minimal influence on the OH that enters the inlet. In addition, the observed OH and HO₂ as well as the ratio of observed-to-modeled OH and HO₂ are uncorrelated with aircraft pitch as it changed from $\sim 2^\circ$ nose down to $\sim 5^\circ$ nose up during several flights on several missions.

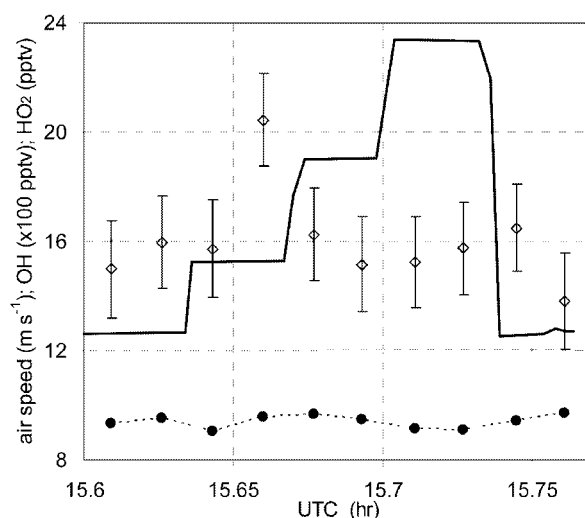


Figure 13. An example from the PEM-Tropics B flight of 15 April, 1999 of the independence of OH measured for varying velocities of ambient air inside the sampling probe's inner nacelle. The solid line is the speed as measured by a pitot tube diametrically across from the inlet. 1-minute averages of OH (open diamonds, 1σ error bars) and HO₂ (solid circles) do not change significantly.

Direct evidence of invariance to airflow velocity comes from in-flight data when the center body within the inner nacelle was moved fore and aft to adjust the ambient air flow across the inlet. The results of ten minutes of such a test are presented in Figure 13 which took place on flight #20 (April 15, 1999) of the PEM-Tropics B mission. Plotted are the ten 1-min observations of OH and HO₂ while the center body was incrementally retracted and then brought back to the full forward position. The air speed is shown by the solid line and was augmented from 12 to 24 m s⁻¹ while the measured ambient OH and HO₂ levels remained relatively constant. The test was performed on a constant altitude leg in which the water vapor, ozone, and NO also remained constant to within 10%.

All of these tests give confidence that losses of OH and HO₂ on the external surfaces of the inlet are negligible. Any small constant losses would, in any event, be taken into account in the calibrations.

5. Absolute Calibration Uncertainties

The sensitivity measured during calibration is the result of carefully measuring all the components of Equations (2) and (3). Aside from the random errors in calibration that determine the precision of the experiment, there are considerable uncertainties in the fixed parameters used to calculate the sensitivity which give rise to possible systematic errors. Table II summarizes the main terms in Equations (2)

Table II. Ranges and uncertainties of the parameters used in the calibration (Equations (2) and (3))

Parameter (units)	Typical values	2 σ Uncertainty
\mathfrak{S}_{185} (photons s ⁻¹ cm ⁻²)	2.4×10^{12}	20%
$\sigma_{\text{H}_2\text{O}}$ (cm ²)	7.14×10^{-20}	6%
[H ₂ O] (per mil)	0.1–30	2%
Δt (ms)	3.5–5.5	16%
P (mW)	0.1–12	18%
$\mathfrak{S}_{185} \times \Delta t$ (photons cm ⁻²)	1.1×10^{10}	27%
C _{OH} (cts s ⁻¹ pptv ⁻¹ mW ⁻¹)	4–40	32%

and (3), typical ranges achieved during calibrations, and estimates of their relative uncertainty.

The largest uncertainty comes from the measurement of the average 185 nm flux in the irradiation zone of the calibrator. The estimated uncertainty in the flux value comes in nearly equal parts from the measurement of the irradiation zone with the phototube, the transfer calibration of the phototube itself, and the combination of flux estimates from the absolute calibration and the two actinic flux methods, as discussed in Sections 3.3 and 3.4. Over time we hope to repeat the process enough times to become more confident in the absolute values and the uncertainties. We use the water photolysis cross section of 7.14×10^{-20} cm² molecule⁻¹ from Cantrell *et al.* (1997), who report their measurement uncertainty of $\pm 6\%$, 2 σ uncertainty. As reported by Cantrell *et al.* (1997), this cross section is some 20–30% different from previously recommended values; however, confirmation of its validity, within the confidence interval, has been made independently by Hofzumahaus *et al.* (1997) and Creasey *et al.* (2000). Specifications of the LI-COR water analyzer (model LI-6262, Lincoln, NE) indicate an accuracy of 2%, and routine calibrations against an optical dew point hygrometer (General Eastern, model 1311DR, Plainville, CT) agree to within 2% from 200–20,000 ppmv. The uncertainty in the irradiation time comes from the measurement of the flux field within the calibrator. Finally the laser power monitored at the output of the White cells are frequently checked against a small filtered photodiode meter (Ophir Optronics, Peabody, MA), and dc electronic zero drifts are tracked by periodically closing the automatic shutter on the Nd:YAG pump laser. The propagation of these estimated systematic errors yields an overall uncertainty in the absolute HO_x measurements of approximately $\pm 32\%$ with 2 σ confidence.

The two actinometric techniques determine directly the overlap of \mathfrak{S}_{185} and Δt . This overlap was $(1.0 \pm 0.1) \times 10^{10}$ photons cm⁻² for N₂O actinometry and $(1.6 \pm 0.2) \times 10^{10}$ photons cm⁻² for O₃ actinometry, with 2 σ uncertainties. In the three calibrations performed with all three techniques so far, the comparisons with

actinometry are encouraging. N₂O actinometry gives an overlap of ≈ 185 and Δt that agrees within 15% with the absolute flux technique, while the O₂ photolysis tends to give a value that is 1.4 times higher than the absolute flux technique. This agreement is within the 2σ uncertainties of the different techniques, although the ozone actinometry is consistently above the other two, implying a systematic error. These differences will likely improve after more calibration and study.

6. Example of the Current ATHOS Detection Limit

The background noise-limited OH detection limit is defined by convention as,

$$[\text{OH}]_{\min} = \frac{(S/N)}{CP} \sqrt{\frac{2}{t}} \sigma_b, \quad (7)$$

where C and P are the instrumental sensitivity and laser power as defined in Equation (3), S/N is the signal-to-noise ratio that determines the minimum, t is the integration time (s), and σ_b is the standard deviation in the background count rate (cts s⁻¹). Equation (7) assumes that the duty cycle is split in half between online and off-resonance measurements, which is how the instrument is usually operated under low OH conditions.

Typical OH sensitivities per mW of laser power are 20 cts s⁻¹ pptv⁻¹ mW⁻¹, with typical background signals of 0.2 cts s⁻¹ mW⁻¹. The typical HO₂ sensitivity per mW is similar, although they are often not identical due to OH wall loss in ATHOS and slight differences in optical collection efficiencies and transmission between the two detection axes. With laser power of 5 mW for the OH axis, the detection sensitivity was typically 80 cts s⁻¹ pptv⁻¹, with a background signal of less than 1 cts s⁻¹. Since only 15% of the laser power is diverted to the HO₂ axis, the typical total HO₂ sensitivity is less than the typical total OH sensitivity.

The detection limits using Equation (7) for one minute integration time and a S/N = 2 are shown for typical operational parameters from the Transport, Radiation, And Chemistry Experiment – Pacific (TRACE-P), which occurred in April–May 2001 (Figure 14). The detection limits of less than 3 ppqv (parts per quadrillion by volume, 10⁻¹⁵) for the middle and upper troposphere calculated here have been verified by laboratory studies using pure air, although not all cylinders of pure air appear to hold pure air. The increase in the detection limits at lower altitudes is due primarily to the additional quenching by water vapor. In this case, the water vapor mixing ratio was ~ 14 per mil. While the detection limits in mixing ratios stabilize above 4 km, as expected, the detection limits in terms of concentration decrease as altitude increases. The detection limit for OH at 10 km is less than 2×10^4 molecules cm⁻³. These low detection limits are well below those necessary to study HO_x chemistry throughout the troposphere and stratosphere.

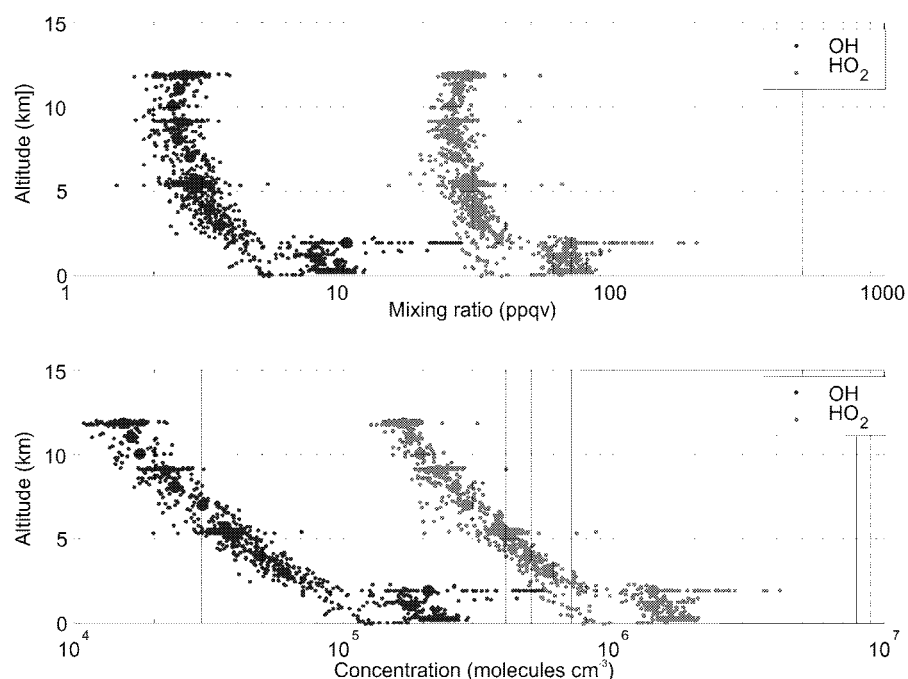


Figure 14. Detection limits for OH and HO₂ versus altitude during TRACE-P, April, 2001. Detection limit, defined by Equation (7), is for 1 minute and $S/N = 2$. The top figure is in mixing ratio (parts per quadrillion by volume, $\text{ppqv} = 10^{-15}$); the bottom figure is in concentration (molecules cm^{-3}).

7. Conclusion

Recent comparisons of ATHOS and GTHOS with other HO_x-measuring instruments have been encouraging, with agreement usually well within the combined 2σ error bars (Eisele *et al.*, 2001; Davis *et al.*, 2001; Eisele *et al.*, 2003; Ren *et al.*, 2003a). Further, our observations of daytime OH and HO₂ have generally agreed with modeled OH and HO₂ to within the 2σ uncertainties of the measurements and models (e.g., Brune *et al.*, 1999; Jaeglé *et al.*, 2001; Tan *et al.*, 2001a; Tan *et al.*, 2001b; Martinez *et al.*, 2003; Ren *et al.*, 2003b). However, the dependences of OH and HO₂ on other atmospheric constituents are not always as expected from theory.

The sensitive detection of atmospheric OH and HO₂, once considered a holy grail of atmospheric composition measurements, has become a reality because of the efforts of several research groups using different detection methods. FAGE is only one of a few successful techniques, but it is now being applied by researchers in several countries around the world. Communication among these researchers can only hasten the improved accuracy, precision, reliability, and versatility of this technique. With these improvements, the understanding of OH and HO₂ will pass from zeroth order, in which the measured and modeled OH and HO₂ are roughly in agreement, to first order, in which the dependences of OH and HO₂ on me-

teology, surfaces, and other atmospheric constituents are precisely understood. This first-order understanding is essential for developing predictive capability for present and future atmospheric oxidation and ozone production. It is the goal of a growing number of researchers who now have the capability to measure atmospheric OH and HO₂.

Acknowledgements

We acknowledge the help of Jeremy Bassis, Terry Shirley, Jennifer Adams, Jingqiu Mao and the fruitful collaborations that we have with colleagues on several airborne and tower-based field intensive studies. We thank Gary Rottman, Ray Wrigley and Ginger Drake at the University of Colorado for the absolute calibrations of our primary standard photomultiplier tube. We also thank our colleagues Frank Holland, Andreas Hofzumahaus, and Dwayne Heard for exchange of information on the FAGE technique. This work has been supported by grants from the National Science Foundation (ATM-9628059, ATM-9974335) and NASA (NAG1-1057, NCC-1-300, NAG2-1117, NAG2-1309, NCC-1-414).

References

- Bailey, A. E., Heard, D. E., Paul, P. H., and Pilling, M. J., 1997: Collisional quenching of OH ($A^2\Sigma^+$, $v' = 0$) by N₂, O₂, and CO₂ between 204 and 294 K, implications for atmospheric measurements of OH by laser-induced fluorescence, *J. Chem. Soc. Faraday Trans.* **93**, 2915–2920.
- Bailey, A. E., Heard, D. E., Henderson, D. A., and Paul, P. H., 1999: Collisional quenching of OH ($A^2\Sigma^+$, $v' = 0$) by H₂O between 211 and 294 K and the development of a unified model for quenching, *Chem. Phys. Lett.* **302**, 132–138.
- Brune, W. H., 1992: Stalking the elusive atmospheric hydroxyl radical, *Science* **256**, 1154–1155.
- Brune, W. H., Stevens, P. S., and Mather, J. H., 1995: Measuring OH and HO₂ in the troposphere by laser-induced fluorescence, *J. Atmos. Sci.* **52**, 3328–3336.
- Brune, W. H., Faloon, I. C., Tan, D., Weinheimer, A. J., Campos, T., Ridley, B. A., Vay, S. A., Collins, J. E., Sachse, G. W., Jaeglé, L., and Jacob, D. J., 1998: Airborne *in situ* OH and HO₂ observations in the cloud-free troposphere and lower stratosphere during SUCCESS, *Geophys. Res. Lett.* **25**, 1701–1704.
- Brune, W. H., Tan, D., Faloon, I., Jaeglé, L., Jacob, D., Heikes, B., Snow, J., Kondo, Y., Shetter, R., Sachse, G., Anderson, B., Gregory, G., Vay, S., Singh, H., Davis, D., Crawford, J., and Blake, D., 1999: OH and HO₂ chemistry in the North Atlantic free troposphere, *Geophys. Res. Lett.* **26**, 3077–3080.
- Cantrell, C. A., Zimmer, A., and Tyndall, G. S., 1997: Absorption cross sections for water vapor from 183 to 193 nm, *Geophys. Res. Lett.* **24**, 2195–2198.
- Copeland, R. A. and Crosley, D. R., 1986: Temperature dependent electronic quenching of OH ($A^2\Sigma^+$, $v' = 0$) between 230 and 310 K, *J. Chem. Phys.* **84**, 3099–3105.
- Creasey, D. J., Halford-Maw, P. A., Heard, D. E., Pilling, M. J., and Whitaker, B. J., 1997: Implementation and initial deployment of a field instrument for measurement of OH and HO₂ in the troposphere by laser-induced fluorescence, *J. Chem. Soc. Faraday Trans.* **93**, 2907–2913.
- Creasey, D. J., Heard, D. E., and Lee, J. D., 2000: Absorption cross-section measurements of water vapour and oxygen at 185 nm, implications for the calibration of field instruments to measure OH, HO₂, and RO₂ radicals, *Geophys. Res. Lett.* **27**, 1651–1654.

- Creasey, D. J., Heard, D. E., and Lee, J. D., 2001: OH and HO₂ measurements in a forested region of north-western Greece, *Atmos. Environ.* **35**, 4713–4724.
- Davis, D. D., Grodzinsky, G., Chen, G., Crawford, J., Eisele, F., Mauldin, L., Tanner, D., Cantrell, C., Brune, W., Tan, D., Faloon, I., Ridley, B., Montzka, D., Walega, J., Grahek, F., Sandholm, S., Sachse, G., Vay, S., Anderson, B., Avery, M., Heikes, B., Snow, J., O'Sullivan, D., Shetter, R., Lefer, B., Blake, D., Blake, N., Carroll M., and Wang, Y., 2001: Marine latitude/altitude OH distributions: Comparison of Pacific Ocean observations with models, *J. Geophys. Res.* **106**, 32,691–32,707.
- Edwards, G. D., Cantrell, C. A., Stephens, S., Hill, B., Goyea, O., Shetter, R. E., Mauldin, R. L., Kosciuch, E., Tanner, D. J., and Eisele, F. L., 2003: Chemical Ionization Mass Spectrometer instrument for the measurement of tropospheric HO₂ and RO₂, *Anal. Chem.* **75**, 5317–5327.
- Eisele, F. L. and Tanner, D. J., 1991: Ion-assisted tropospheric OH measurements, *J. Geophys. Res.* **96**, 9295–9308.
- Eisele, F. L. and Bradshaw, J. D., 1993: The elusive hydroxyl radical: Measuring OH in the atmosphere, *Anal. Chem.* **65**, 927–939.
- Eisele, F. L., Mauldin, L., Tanner, D. J., Cantrell, C., Kosciuch, E., Brune, W., Faloon, I., Tan, D., Davis, D. D., and Chen, G., 2001: The relationship between P-3B and DC-8 OH measurements during PEM-Tropics B, *J. Geophys. Res.* **106**, 32,683–32,689.
- Eisele, F. L., Mauldin, L., Cantrell, C., Zondlo, M., Apel, E., Fried, A., Walega, J., Shetter, R., Lefer, B., Flocke, F., Weinheimer, A., Avery, M., Vay, S., Sachse, G., Podolske, J., Diskin, G., Barrick, J. D., Singh, H. B., Brune, W., Harder, H., Martinez, M., Bandy, A., Thornton, D., Heikes, B., Kondo, Y., Riemer, D., Sandholm, S., Tan, D., Talbot, R., and Dibb, J., 2003: Summary of measurement intercomparisons during TRACE-P, *J. Geophys. Res.* **108**, 8791, doi:10.1029/2002JD003167.
- Faloon, I., Tan, D., Brune, W., Hurst, J., Barket Jr., D., Couch, T. L., Shepson, P., Apel, E., Riemer, D., Thornberry, T., Carroll, M. A., Sillman, S., Keeler, G. J., Sagady, J., Hooper, D., and Paterson, K., 2001: Nighttime observations of anomalously high levels of hydroxyl radicals above a deciduous forest canopy, *J. Geophys. Res.* **106**, 24,315–24,333.
- Hard, T. M., O'Brien, R. J., Chan, C. Y., Mehrabzadeh, A. A., 1984: Tropospheric free radical determination by FAGE, *Environ. Sci. Technol.* **18**, 768–777.
- Hard, T. M., Chan, C. Y., Mehrabzadeh, A. A., and O'Brien, R. J., 1992: FAGE measurements of tropospheric HO with measurements and model of interferences, *J. Geophys. Res.* **97**, 9795–9817.
- Heal, M. R., Heard, D. E., Pilling, M. J., and Whitaker, B. J., 1995: On the development and validation of FAGE for local measurements of tropospheric OH and HO₂, *J. Atmos. Sci.* **52**, 3428–3441.
- Hofzumahaus, A., Aschmutat, U., Heßling, M., Holland, F., and Ehhalt, D. H., 1996: The measurement of tropospheric OH radicals by laser-induced fluorescence spectroscopy during the POPCORN field campaign, *Geophys. Res. Lett.* **23**, 2541–2544.
- Hofzumahaus, A., Brauers, T., Aschmutat, U., Brandenburger, U., Dorn, H.-P., Hausmann, M., Heßling, M., Holland, F., Plass-Dülmer, C., Sedlacek, M., Weber, M., and Ehhalt, D. H., 1997: Reply to comment by Lanzendorf *et al.*, *Geophys. Res. Lett.* **24**, 3039–3040.
- Holland, F., Heßling, M., and Hofzumahaus, A., 1995: *In situ* measurement of tropospheric OH radicals by laser-induced fluorescence – a description of the KFA instrument, *J. Atmos. Sci.* **52**, 3393–3401.
- Holland, F., Aschmutat, U., Hessling, M., Hofzumahaus, A., and Ehhalt, D. H., 1998: Highly time resolved measurements of OH during POPCORN using laser-induced fluorescence spectroscopy, *J. Atmos. Chem.* **31**, 205–225.
- Holland, F., Hofzumahaus, A., Schäfer, J., Kraus, A., and Pätz, H., 2003: Measurements of OH and HO₂ radical concentrations and photolysis frequencies during BERLIOZ, *J. Geophys. Res.* **108**, 8246, doi: 10.1029/2001JD001393.

- Jaeglé, L., Jacob, D. J., Brune, W. H., and Wennberg, P. O., 2001: Chemistry of HO_x radicals in the upper troposphere. *Atmos. Environ.* **35**, 469–489.
- Kanaya, Y., Sadanaga, Y., Matsumoto, J., Sharma, U. K., Hirokawa, J., Kajii, Y., and Akimoto, H., 1999: Nighttime observation of the HO₂ radical by a LIF instrument at Oki island, Japan, and its possible origins. *Geophys. Res. Lett.* **26**, 2179–2183.
- Lanzendorf, E. J., Hanisco, T. F., Donahue, N. M., and Wennberg, P. O., 1997: Comment on: ‘The measurement of tropospheric OH radicals by laser-induced fluorescence spectroscopy during the POPCORN field campaign’ by Hofzumahous *et al.* and ‘Intercomparison of tropospheric OH radical measurements by multiple folded long-path laser absorption and laser induced fluorescence’ by Brauers *et al.*, *Geophys. Res. Lett.* **24**, 3037–3038.
- Levenberg, K., 1944: A method for the solution of certain problems in least squares, *Quart. Appl. Math.* **2**, 164–168.
- Levy II, H., 1971: Normal atmosphere: Large radical and formaldehyde concentrations predicted, *Science* **173**, 141–143.
- Marquardt, D., 1963: An algorithm for least-squares estimation of nonlinear parameters, *SIAM J. Appl. Math.* **11**, 431–441.
- Martinez, M., Harder, H., Kovacs, T. A., Simpas, J. B., Bassis, J., Leshner, R., Brune, W. H., Frost, G., Williams, E. J., Stroud, C. A., Jobson, B. T., Roberts, J. M., Hall, S. R., Shetter, R. E., Wert, B., Fried, A., Alicke, B., Stutz, J., Young, V. L., White, A. B., and Zamora, R. J., 2003: OH and HO₂ concentrations, sources and loss rates during the Southern Oxidants Study in Nashville, TN, summer 1999, *J. Geophys. Res.* **108**, 4617, doi:10.1029/2003JD003551.
- Mather, J. H., Stevens, P. S., and Brune, W. H., 1997: OH and HO₂ measurements using laser-induced fluorescence, *J. Geophys. Res.* **102**, 6427–6436.
- McConnell, J. C., McElroy, M. B., and Wofsy, S. C., 1971: Natural sources of atmospheric CO, *Nature* **233**, 187–188.
- Mount, G. H. and Harder, J. W., 1995: The measurement of tropospheric trace gases at Fritz Peak Observatory, Colorado, by Long-Path Absorption: OH and ancillary gases, *J. Atmos. Sci.* **52**, 3342–3353.
- Ortgies, G., Gericke, K.-H., and Comes, F. J., 1981: Optical measurements of tropospheric hydroxyl with lasers, *Z. Naturforsch.* **36a**, 177–183.
- Perner, D., Paltt, U., Trainer, M., Huebler, G., Drummond, J. W., Junkermann, W., Rudolph, J., Schubert, B., Volz-Thomas, A., Ehhalt, D. H., Rumpel, K. J., and Helas, G., 1987: Measurement of tropospheric OH concentrations: A comparison of field data with model predictions, *J. Atmos. Chem.* **5**, 185–216.
- Ren, X., Edwards, G. D., Cantrell, C. A., Leshner, R. L., Metcalf, A. R., Shirley, T., and Brune, W. H., 2003a: Intercomparison of peroxy radical measurements at a rural site using laser-induced fluorescence and Peroxy Radical Chemical Ionization Mass Spectrometer (PerCIMS) techniques, *J. Geophys. Res.* **108**, 4605, doi:10.1029/2003JD003644.
- Ren, X., Harder, H., Martinez, M., Leshner, R. L., Oligier, A., Simpas, J. B., Brune, W. H., Schwab, J. J., Demerjian, K. L., He, Y., Zhou, X., and Gao, H., 2003b: OH and HO₂ chemistry in the urban atmosphere of New York City, *Atmos. Environ.* **37**, 3639–3651.
- Ren, X., Harder, H., Martinez, M., Faloon, I., Tan, D., Leshner, R. L., DiCarlo, P., Simpas, J. B., and Brune, W. H., 2004: Interference testing for Atmospheric HO_x measurements by laser-induced fluorescence, *J. Atmos. Chem.* **47**, 169–190.
- Sander, S. P., Friedl, R. R., DeMore, W. B., Golden, D. M., Kurylo, M. J., Hampson, R. F., Huie, R. E., Moortgat, C. K., Ravishankara, A. R., Kolb, C. E., and Molina, M. J., 2000: Chemical kinetics and photochemical data for use in stratospheric modeling, Evaluation number 12, *JPL Publication 00–3*, NASA Jet Propulsion Laboratory, Pasadena, California.
- Schultz, M., Heitlinger, M., Mihelcic, D., and Volz-Thomas, A., 1995: Calibration source for peroxy radicals with built-in actinometry using H₂O and O₂ photolysis at 185 nm, *J. Geophys. Res.* **100**, 18,811–18,816.

- Stevens, P. S., Mather, J. H., and Brune, W. H., 1994: Measurement of tropospheric OH and HO₂ by laser-induced fluorescence at low pressure, *J. Geophys. Res.* **99**, 3542–3557.
- Tan, D., Faloon, I., Simpas, J. B., Brune, W., Shepson, P. B., Couch, T. L., Sumner, A. L., Carroll, M. A., Thornberry, T., Apel, E., Riemer, D., and Stockwell, W., 2001a: HO_x budget in a deciduous forest: Results from the PROPHET summer 1998 campaign, *J. Geophys. Res.* **106**, 24407–24427.
- Tan, D., Faloon, I., Simpas, J. B., Brune, W., Olson, J., Crawford, J., Avery, M., Sachse, G., Vay, S., Sandholm, S., Guan, H.-W., Vaughn, T., Mastromarino, J., Heikes, B., Snow, J., Podolske, J., and Singh, H., 2001b: OH and HO₂ in the tropical Pacific: Results from PEM-Tropics B, *J. Geophys. Res.* **106**, 32,667–32,681.
- Tanner, D. J. and Eisele, F. L., 1995: Present OH measurement limits and associated uncertainties, *J. Geophys. Res.* **100**, 2883–2892.
- Wennberg, P. O., Cohen, R. C., Hazen, N. L., Lapson, L. B., Allen, N. T., Hanisco, T. F., Oliver, J. F., Lanham, N. W., Demusz, J. N., and Anderson, J. G., 1994: Aircraft-borne, laser-induced fluorescence instrument for the *in situ* detection of hydroxyl and hydroperoxyl radicals, *Rev. Sci. Instr.* **65**, 1858–1876.
- Wennberg, P. O., Hanisco, T. F., Cohen, R. C., Stimpfle, R. M., Lapson, L. B., and Anderson, J. G., 1995: *In situ* measurements of OH and HO₂ in the upper troposphere and stratosphere, *J. Atmos. Sci.* **52**, 3413–3420.
- White, J., 1942: Long optical paths of large aperture, *J. Opt. Soc. Amer.* **32**, 285–288.
- Wysong, I. J., Jeffries, J. B., and Crosley, D. R., 1990: Quenching of A²Σ⁺ OH at 300 K by several colliders, *J. Chem. Phys.* **92**, 5218–5222.